J Adv Ceram

Research Article

Avoiding undesirable cathode/electrolyte interfacial reactions for proton-conducting solid oxide fuel cells by Joule heating

Yiheng Gu[1], Zhiyu Chen[1], Zhicheng Wang[1], Shoufu Yu[2], Lei Bi[2,✉]

Cite this article: Gu Y, Chen Z, Wang Z, et al. *J Adv Ceram* 2025, **14**(3): 9221040. https://doi.org/10.26599/JAC.2025.9221040

ABSTRACT: The co-firing stage is an unavoidable step in the fabrication process of solid oxide fuel cells (SOFCs), and avoiding unwanted interfacial reactions is crucial for cathode construction during the co-firing process. In this study, $LiMn_2O_4$ (LiMO), a traditional electrode material for Li-ion batteries, was discovered to have protonation and proton diffusion properties, showing significant promise as a cathode for proton-conducting SOFCs (H-SOFCs). However, obvious interactions between the LiMO cathode and $BaCe_{0.7}Zr_{0.1}Y_{0.2}O_{3-\delta}$ (BCZY) electrolyte can be identified during the co-firing process using the conventional sintering method, resulting in poor performance and making the use of LiMO in H-SOFCs challenging. To address this issue, the Joule heating process is used to produce the LiMO cathode for H-SOFCs. In contrast to the traditional co-firing process, which takes a few hours, the Joule heating method, which completes the co-sintering procedure in a few seconds, can successfully bind the LiMO to the BCZY electrolyte with no visible interlayer reactions or elemental diffusions. As a result, the full potential of LiMO for H-SOFCs is realized, resulting in a high fuel cell output of 1426 mW·cm^{-2} at 700 °C, approximately double that of the cell utilizing the normally sintered LiMO cathode. To the best of our knowledge, this is the first study to use Joule heating to prevent the cathode/electrolyte interfacial reaction in H-SOFCs, which presents an interesting approach for manufacturing and may also breathe new life into some materials that are previously incompatible with H-SOFCs.

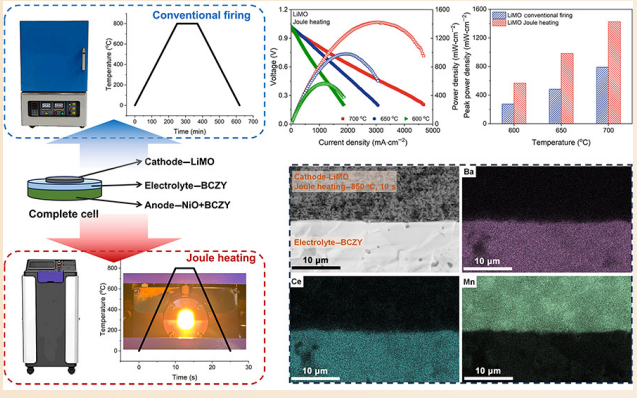

KEYWORDS: Joule heating; cathode; interlayer; proton-conducting oxides; solid oxide fuel cells

1 Introduction

The development of sustainable materials and technologies is required to address the current energy and environmental challenges worldwide [1–5]. Various techniques have been proposed, with fuel cells receiving significant attention because of their high efficiency and low level of pollution while converting fuel energy into electricity [6,7]. Various types of fuel cells exist, and solid oxide fuel cells (SOFCs) are fuel cells that use oxides as their primary components, preventing liquid leakage and providing fuel flexibility [8–10]. Furthermore, metal oxides, rather than noble metals, are employed as electrode catalysts in SOFCs, lowering the cost of fuel cells [11]. Despite these benefits, SOFCs have several drawbacks since the operating temperature for traditional SOFCs is excessively high (over 800 °C). The high working temperature limits the lifetime of fuel cells and makes it difficult to choose appropriate compatible materials [12]. As a result, the primary goal of the SOFC community is to construct SOFCs capable of operating at intermediate temperatures [13–15].

Proton-conducting SOFCs (H-SOFCs), which are SOFCs with proton-conducting electrolytes [16] represent a potential alternative for lowering the working temperature of conventional SOFCs [17]. Owing to the low activation and high ionic conductivity of proton-conducting electrolytes [18], using them as electrolytes can efficiently reduce a cell's ohmic resistance, allowing SOFCs to operate at lower temperatures. However, despite the lower electrolyte resistance associated with the use of proton-conducting electrolytes [19], the polarization resistance of traditional cathodes becomes dominant at intermediate temperatures, as the cathode reaction kinetics are dramatically reduced at reduced operation temperatures [20]. As a result, one of the most actively researched subjects in the H-SOFC field is the development of high-performance cathodes at intermediate temperatures [21,22].

The reaction mechanism of H-SOFC cathodes demonstrates that proton migration is crucial to cathode performance [23,24]. In recent years, several high-performance cathodes have been developed with a focus on increasing the degree of protonation of

[1] School of Electronic and Information Engineering, Changshu Institute of Technology, Changshu 215500, China. [2] School of Resource Environment and Safety Engineering, University of South China, Hengyang 421001, China.

✉ Corresponding author. E-mail: lei.bi@usc.edu.cn, bilei81@gmail.com

Received: November 18, 2024; Revised: January 2, 2025; Accepted: January 19, 2025

the cathode material [25]. Notably, the majority of these high-performance cathodes are based on perovskite oxides [26], with few studies on other oxides. Although the flexibility in tweaking the properties of perovskite oxides has allowed them to become the most researched material system in the field [27,28], further examination of alternative cathode oxides may yield new candidates for H-SOFC cathodes [29]. Some recent research suggests that lithiated oxides hold considerable promise as cathodes for H-SOFCs because of their potential protonation [30,31]. However, it should be noted that a co-firing procedure is required during SOFC fabrication to provide a proper connection between the cathode and electrolyte, and this process is often carried out in a high-temperature furnace at high temperatures for several hours. At high temperatures, several lithiated oxides react with proton-conducting electrolytes [30]. Furthermore, the high-temperature calcination method can cause Li evaporation in lithiated oxides [32]. These issues must be addressed before the practical implementation of lithiated oxide cathodes in H-SOFCs. To address this issue, Joule heating, an ultrafast sintering process, is used to resolve the interfacial reaction problem between the lithiated oxide cathode and proton-conducting electrolyte. $LiMn_2O_4$ (LiMO) was chosen as the lithiated oxide cathode in the present study because of its low toxicity, low cost, and high natural Mn abundance [33]. Furthermore, LiMO is a mature Li-ion battery electrode that can bridge the gap in material selection between Li-ion batteries and H-SOFCs. In this study, LiMO oxide was used as a cathode for H-SOFCs, with the goal of broadening the range of cathode materials available. The cathode construction procedure was carried out utilizing conventional sintering and Joule heating. The different interfacial reactions and their impacts on fuel cell performance were investigated.

2 Materials and methods

LiMO oxide was produced using the sol–gel technique. Li_2CO_3 was dissolved in nitric acid, and $Mn(OOCCH_3)_2$ was employed as a Mn source. Citric acid was utilized as the complexing agent, and the final pH of the solution was set to approximately 8. All chemicals were purchased from Aladdin Scientific, China. The solution was heated to approximately 80 °C to evaporate water and produce the precursors. The LiMO precursor was heated at 800 °C for 3 h to produce the target material. The phase purity of the produced material was determined using an X-ray diffractometer (XRD; X′ pert3, PANalytical) at a scan rate of 3 (°)·min^{-1}. The structure of the LiMO material was further analyzed using a transmission electron microscope (TEM; JEM-2100F, JEOL). The conductivity of the material was measured using a direct current (DC) four-probe method using a digital meter (Keithley 2010). Dense LiMO bars were prepared, which were connected to four leading wires. Two outer probes were connected to a current source, and two inner probes were connected to the digital meter to measure the voltage drop across the material. Electrical conductivity relaxation (ECR) was carried out to study the proton diffusion ability of LiMO. The conductivity of LiMO was first measured in dry air, and the testing condition was abruptly changed to wet air (3% H_2O). Then, the relaxation time for reaching a new conductivity equilibrium was recorded. The thermal expansion coefficient (TEC) of LiMO from room temperature to 900 °C was measured via a dilatometer (Netzsch DIL 402E) in an air atmosphere. The hydration ability of LiMO was investigated via a thermogravimeter (TG; Netzsch STA 449). The LiMO material was tested under dry and wet air conditions, and the weight difference can be used to determine the hydration capacity of LiMO [34].

To study the suitability of LiMO as a cathode for H-SOFCs, first-principles calculations using density functional theory (DFT) were performed at the atomic level. The VASP program was utilized [35]. We employed the climbing-image nudged elastic band (CI-NEB) [36] approach to investigate proton migration. The cutoff energy was set at 520 eV. The energy and force convergence requirements were established at 10^{-5} eV and 0.05 eV·Å^{-1}, respectively. A gamma centered 4 × 4 × 4 *k*-point mesh was chosen to describe the Brillouin zone. For Hubbard's correction, a U_{eff} value of 3.9 eV was set for Mn.

Fuel cells with BCZY proton-conducting electrolytes were constructed to test the performance of LiMO as a cathode for H-SOFCs. A co-pressing approach was used to generate anode-supported half cells with a BCZY electrolyte layer produced on the NiO+BCZY anode substrate. The NiO+BCZY/BCZY green bilayers were co-sintered at 1350 °C for 6 h to densify the supporting BCZY electrolyte. The cathode ink was made of LiMO powder, ethyl cellulose, and terpineol at a weight ratio of 10 : 1 : 10. The ethyl cellulose in the cathode ink was used as the pore former. The LiMO cathode slurry was then placed on the dense BCZY electrolyte, which was fired alongside the half-cell to build the whole cell. Two alternative co-firing systems were utilized. One is typical high-temperature co-firing in a muffle furnace, which takes several hours to complete. The other method is to use Joule heating to co-fire the cathode with the half-cell, which results in co-firing in a few seconds [37]. Joule heating is the process by which electrical energy is converted into heat when an electric current flows through a conductor with resistance. This phenomenon occurs because of collisions between the flowing electrons and atoms or molecules in the material, which causes energy loss in the form of heat. The heat generated is proportional to the square of current and resistance of the material: $P = I^2R$, where P is the heat generated; I is the current; R is the resistance. Joule heating can achieve fast heating because the electrical energy is directly converted into heat in the material with minimal delay. When the current is stopped, heat generation stops, and the material begins to cool instantly. In this study, a Joule heating equipment (CIS-JH3.3-P) was purchased from Hefei *In-situ* Technology Co., Ltd. The system schematic is shown in Fig. 1. The graphite plate served as a sample holder during the Joule heating procedure. The entire Joule heating process was carried out under vacuum to avoid oxidation of the graphite plate holder. The voltage utilized for Joule heating was modified to maintain the current at 150 A. The temperature of the sample was detected with an infrared thermometer. Following the Joule heating technique, the entire cell was heated at 500 °C for 2 h in a standard muffle furnace to remove any organic compounds and carbon that could not be eliminated during Joule heating. To investigate the possibility of a cathode/electrolyte interfacial reaction, a cross-section of the

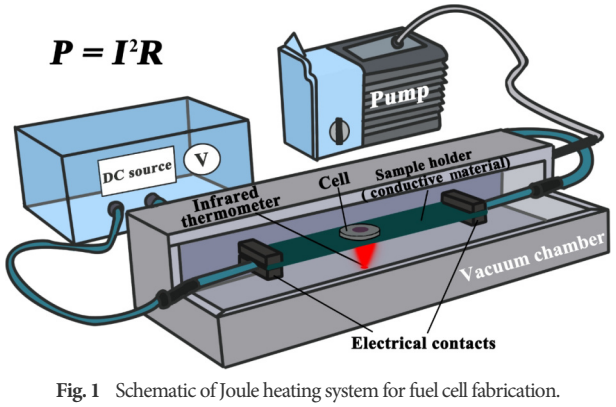

Fig. 1 Schematic of Joule heating system for fuel cell fabrication.

cathode/electrolyte interface was observed by scanning electron microscopy (SEM; Phenom XL, Thermo Scientific). An energy dispersive spectrometer (EDS; FAST SDD 123, AMPTEK) coupled with the Phenom elemental identification system was used to investigate the element distribution at the interface following co-firing. The fuel cells were made of NiO+BCZY anodes (approximately 0.5 mm thick), BCZY electrolytes (approximately 14 μm thick), and LiMO cathodes (approximately 35 μm thick). Ag paste was used as a current collector for the cathode. The performance of fuel cells with LiMO cathodes manufactured under various conditions was assessed under fuel cell operating conditions. Wet H_2 was employed as fuel, whereas static air was used as an oxidant. The fuel cell output was measured using an electrochemical workstation (SquidStat Plus, Admiral Instrument) via linear sweep voltammetry. The scan rate was set at 10 $mV \cdot s^{-1}$. Electrochemical impedance spectroscopy (EIS) was employed to analyze the resistance of the cell under open-circuit voltage conditions with a frequency range from 1 MHz to 0.1 Hz, and the alternating current (AC) excitation amplitude was set at 10 mV.

3 Results and discussion

Figure 2(a) depicts the XRD pattern of the as-prepared LiMO material. The LiMO exhibits a pure phase with no identifiable impurities, which is consistent with the standard LiMO in the database. Figure 2(b) shows the Rietveld refinement of the XRD data used to acquire crystal structure information for LiMO. The LiMO is attributed to a cubic structure with the space group $Pm\bar{3}m$. Based on the reliable parameters of $\chi^2 = 1.19$, $R_p = 3.61\%$, and $R_{wp} = 4.82\%$, the lattice parameters are $a = b = c = 8.41$ Å. The high-resolution TEM (HR-TEM) images in Fig. 2(c) also provide the crystal structure information of LiMO, according to the interplanar spacings of 4.21, 4.86, 4.86, and 2.97 Å corresponding to the crystallographic planes of $(00\bar{2})$, $(11\bar{1})$, $(\bar{1}\bar{1}\bar{1})$, and $(\bar{2}\bar{2}0)$, respectively, and the lattice parameters are calculated to be $a = b = c = 8.42$ Å, which is consistent with the refinement results. Notably, although no extra Li was employed to compensate for any Li evaporation, pure-phase LiMO was still achieved, which was probably due to the relatively low calcination temperature of 800 °C.

The suitability of LiMO as a cathode for H-SOFCs was next explored using DFT simulations. Figure 3(a) depicts the calculated structure of LiMO. The computed lattice value, $a = b = c = 8.45$ Å, aligns with the XRD analysis results. Figure 3(b) depicts the potential oxygen reduction reaction (ORR) of LiMO as measured by the distance between the O p-band center and the Fermi level. The distance between the O p-band center and the Fermi level highlights the difficulty of adding and removing electrons between the O p-band center and the Fermi level, which are fundamental steps in O addition and removal that influence many important features of ORR. As a result, this distance value is considered an

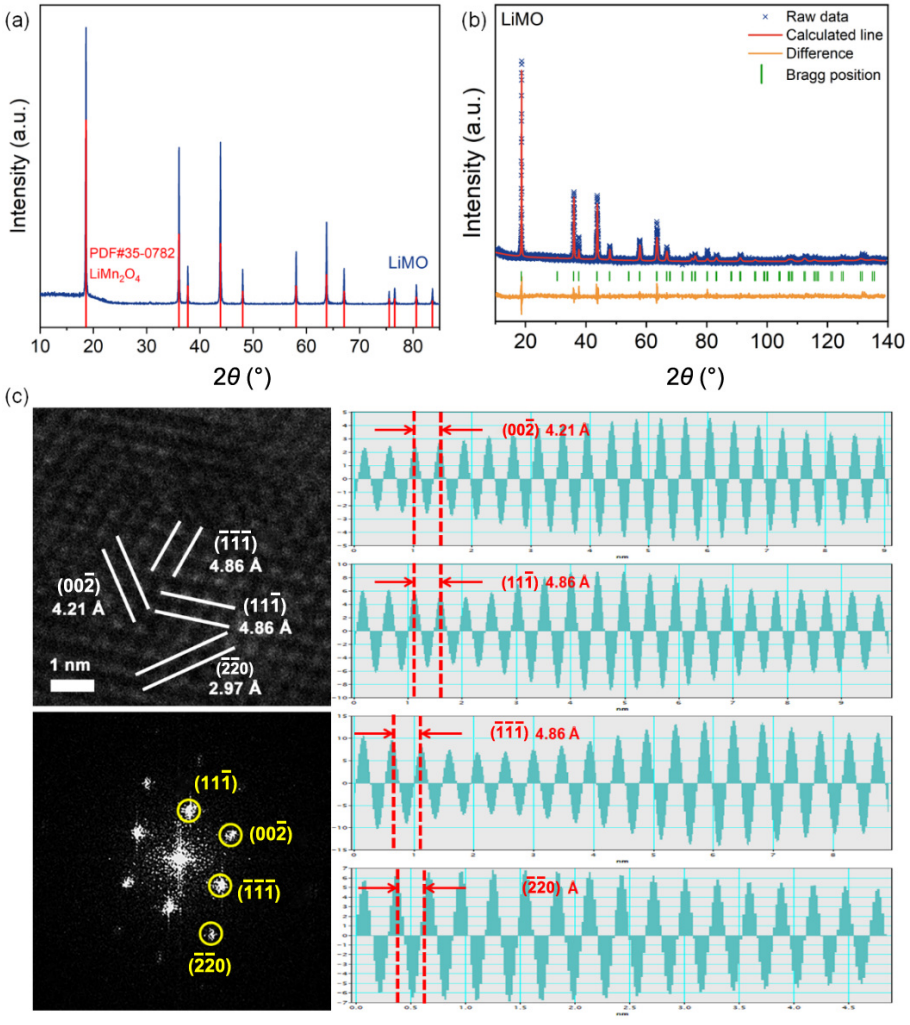

Fig. 2 (a) XRD, (b) Rietveld refinement, and (c) HR-TEM images with diffraction spots for LiMO.

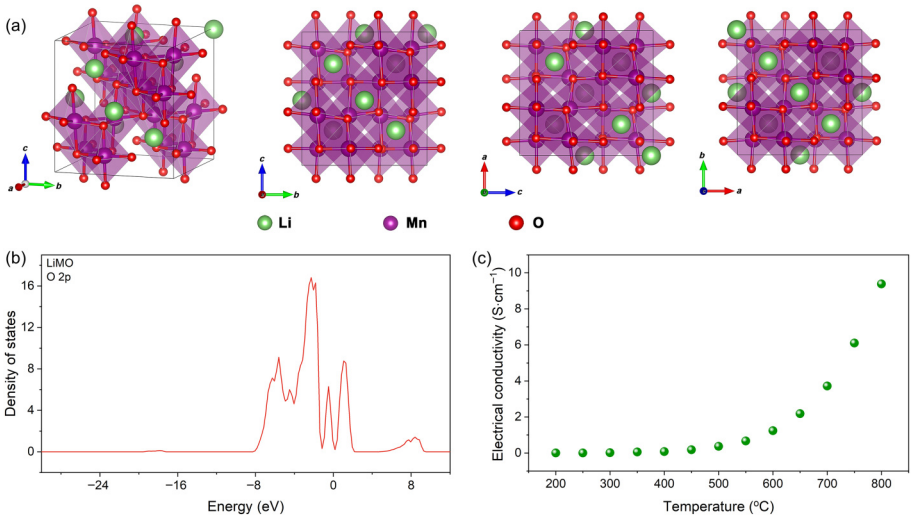

Fig. 3 (a) Calculated structure, (b) O projected density of states (p-DOS), and (c) conductivity of LiMO.

appropriate descriptor for the ORR activity of oxide cathodes in SOFCs [38]. The distance is 2.52 eV, which is comparable to that of Sr-doped $LaCoO_3$ [38], a highly active cathode for traditional SOFCs, showing that LiMO oxide may have adequate ORR activity as a prospective SOFC cathode. According to reports, the cathode process for H-SOFCs involves the participation of oxygen ions, protons, and electrons [23]. Better oxygen addition and removal abilities imply greater oxygen-ion migration abilities, which improve cathode performance even in H-SOFCs. The conductivity of LiMO was further investigated using a DC four-probe method, and the results are presented in Fig. 3(c). The conductivity of LiMO is not as high as that of some oxide cathodes, but it still reaches a few $S{\cdot}cm^{-1}$ at intermediate temperatures, making it suitable as a cathode for SOFCs [39]. In addition, the thickness of the cathode is only approximately 35 μm, as shown in Fig. S1 in the Electronic Supplementary Material (ESM), which makes the overall resistance of the cathode layer small. The foregoing results show that the LiMO material has adequate conductivity and possible ORR activity, which meets the general criteria for a cathode in SOFCs. However, protonation is crucial for the specific design of cathodes for H-SOFCs since a cathode with enough protonation can increase the reaction active area [40,41], improving cathode performance. Therefore, the possible protonation of LiMO is studied.

Protonation occurs in oxides due to the interaction of Vo and H_2O, which can be expressed as $H_2O + V_o^{\cdot\cdot} + O_o^x \rightarrow 2OH^{\cdot}$ [42]. As a result, the protonation ability is determined by its hydration. The hydration energy (E_{hydra}) is calculated according to $E_{hydra} = E_{2OH} - E_{defect} - E_{H_2O}$, where E_{2OH} is the energy of the crystal with two additional protons; E_{defect} is the total energy of the defective bulk; E_{H_2O} is the energy of a single water molecule. The E_{hydra} of LiMO is predicted to be −0.24 eV, indicating that hydration is beneficial in LiMO. After proton defects are formed, fast proton mobility is highly desirable. As a result, the proton migration in LiMO is simulated. Proton migration in oxides involves two steps: rotating and hopping [43], as shown in Fig. 4(a). The proton rotates within the oxygen atom before hopping to the adjacent oxygen atom, initiating the proton transportation process. The energy barriers for the rotating and hopping steps in LiMO are 0.14 and 0.81 eV, respectively, indicating that the hopping step is the potential limiting step in proton migration in LiMO, which is consistent with Ref. [43]. Although the DFT calculation is based on the energies at the ground state, it is still useful for predicting the properties at high temperatures. At elevated temperatures, the properties of a system are governed by statistical mechanics. The ground-state energy forms the baseline for calculating the free energy at high temperatures. In addition, some materials retain their structural and electronic features determined at the ground state over a wide temperature range, making DFT predictions reasonable even at elevated temperatures. Therefore, many studies use DFT calculations to predict the properties of key SOFC materials [21,27,38]. The energy barrier for proton hopping is similar to that reported for several perovskite cathodes with proton conduction [44,45], indicating the possibility of proton migration in LiMO. In contrast, the degree of oxygen migration in LiMO is poor, as evidenced by the DFT calculations of oxygen migration. The energy barrier for oxygen transportation is 4.47 eV, which is substantially higher than that for proton transport, implying that proton migration is more advantageous than oxygen migration in LiMO. The hydration of LiMO and the proton diffusion in the material are further studied experimentally using TG and electrical conductivity relaxation (ECR) measurements. The LiMO powder was first treated at 800 °C for 2 h to remove the adsorbed H_2O from the material. The LiMO material was then treated under both dry and moist air conditions, and the weight was measured using the TG method, as shown in Fig. 4(b). Weight gain can be observed in both atmospheres. As the temperature decreases, LiMO adsorbs O_2 in dry air, resulting in an increase in weight. However, the weight rise in a wet atmosphere is clearly greater than that in dry air condition, indicating the hydration behavior of LiMO in a wet environment [34]. The apparent hydration ability of LiMO is consistent with its low E_{hydra}, indicating that hydration in LiMO is favorable. The ability of proton diffusion is explored experimentally using ECR measurements. Figure 4(c) depicts the ECR curve of LiMO in an atmosphere that transitions from dry to moist air. Owing to the introduction of H_2O into the atmosphere, the development of proton defects can alter the conductivity of a material, and the time required to establish a new conductivity equilibrium represents the proton diffusion capacity [46]. The relaxation period is approximately 650 s, which is faster than that of many previously reported H-SOFC cathodes [47,48], implying faster proton diffusion kinetics. Fitting the ECR curve yielded D_H and K_H values of $1.02{\times}10^{-4}$ $cm^2{\cdot}s^{-1}$ and $1.43{\times}10^{-3}$ $cm{\cdot}s^{-1}$, respectively. The apparent proton diffusion ability of LiMO is consistent with the relatively low E_{rot} and E_{hop} values determined by the DFT technique. According to the studies mentioned above, LiMO not

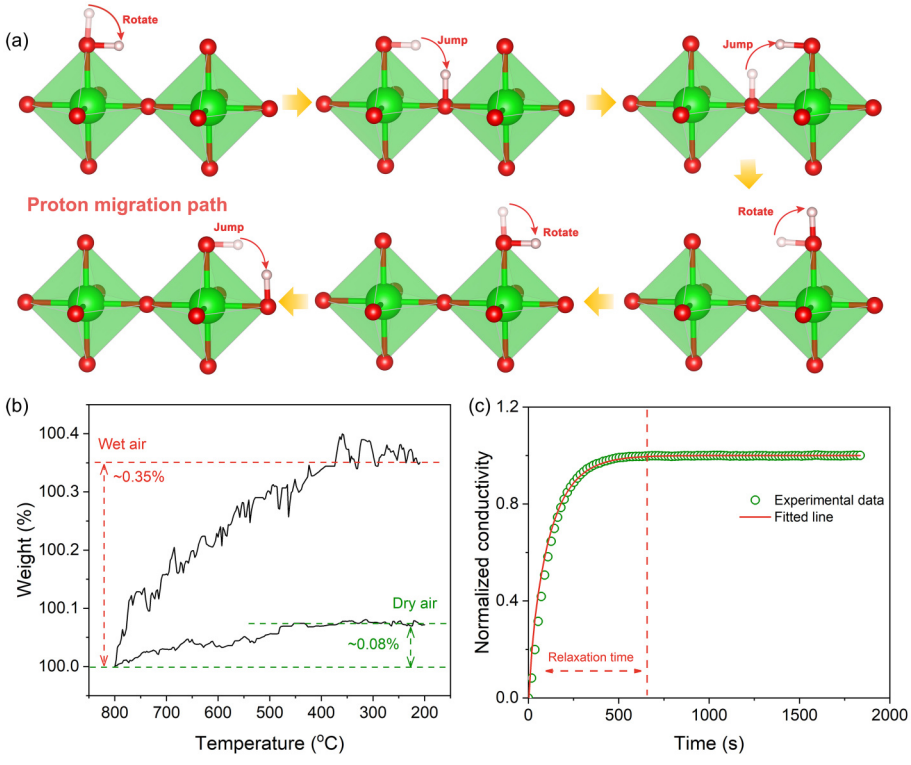

Fig. 4 (a) Schematic for proton migration in oxides; (b) TG curves for LiMO in dry and wet air conditions; (c) ECR curve of LiMO in the atmosphere abruptly changing from dry to wet air.

only has good conductivity and prospective ORR ability but also has protonation and proton migration abilities, which make it very promising for H-SOFC applications.

Therefore, the LiMO cathode is constructed on BCZY electrolyte-based half-cells. During the cathode fabrication process, LiMO is deposited on the electrolyte surface and must be co-fired with the half-cell, as shown in Fig. 5. The co-firing procedure involves two methods: conventional sintering and Joule heating. The conventional sintering technique has a slow heating rate, reaching only a few °C·min^{-1}. In addition, the entire cell must be held at a high temperature for a few hours to provide a good connection between the cathode and electrolyte. As a result, the whole cathode fabrication procedure typically takes a few to tens of hours. In comparison, employing Joule heating reduces the entire cathode production process to tens of seconds. The Joule heating method allows for exceptionally fast heating and cooling, and the sample is only kept at high temperatures for very short time.

Therefore, co-firing can be completed in significantly less time than the time of conventional sintering, which may have various effects on the cathode/electrolyte interfaces. Figure 6(a) depicts a SEM cross-sectional image of the cell with a typically sintered LiMO cathode. After co-firing at 800 °C for 2 h, LiMO is connected to the electrolyte, resulting in the typical tri-layer structure of the fuel cell. However, an obvious interfacial reaction could be detected at the LiMO cathode/BCZY electrolyte contact, implying that a reaction between LiMO and BCZY occurs during the co-firing procedure when the conventional sintering technique is used. Figure 6(b) depicts the XRD patterns of LiMO+BCZY composite powder before and after co-firing at 800 °C for 2 h in a typical high-temperature furnace. In addition to the peaks corresponding to LiMO and BCZY, several additional peaks, primarily associated with $BaMnO_3$, appear. This finding demonstrates that there is a reation between LiMO and BCZY following co-firing using the conventional sintering process. The

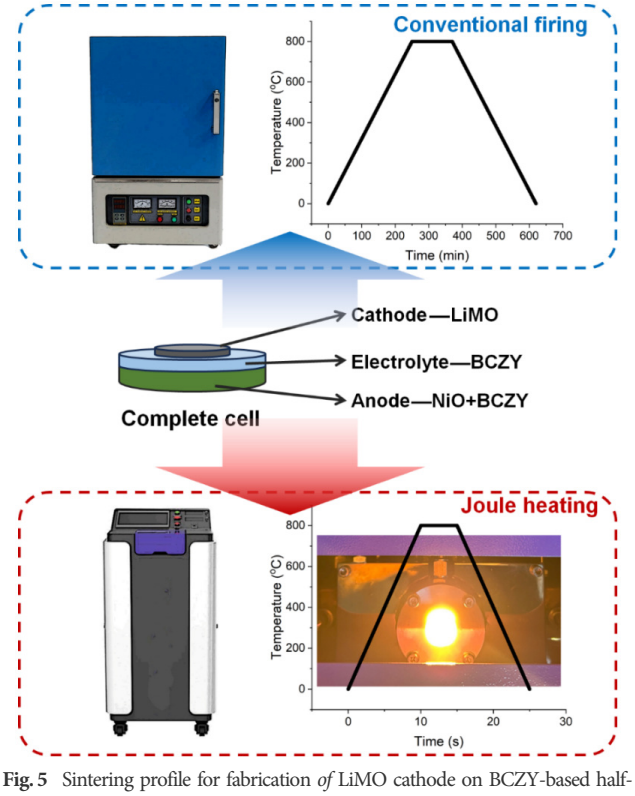

Fig. 5 Sintering profile for fabrication *of* LiMO cathode on BCZY-based half-cells by using conventional sintering and Joule heating.

elemental mapping results, given in Fig. 6(c), illustrate that the interfacial reaction causes elemental diffusion at the interface. A portion of Ba element migrates from the BCZY electrolyte layer to LiMO cathode layer, creating a Ba-rich layer in the LiMO cathode. Because of Ba migration, an obvious layer of Ba deficit and Ce

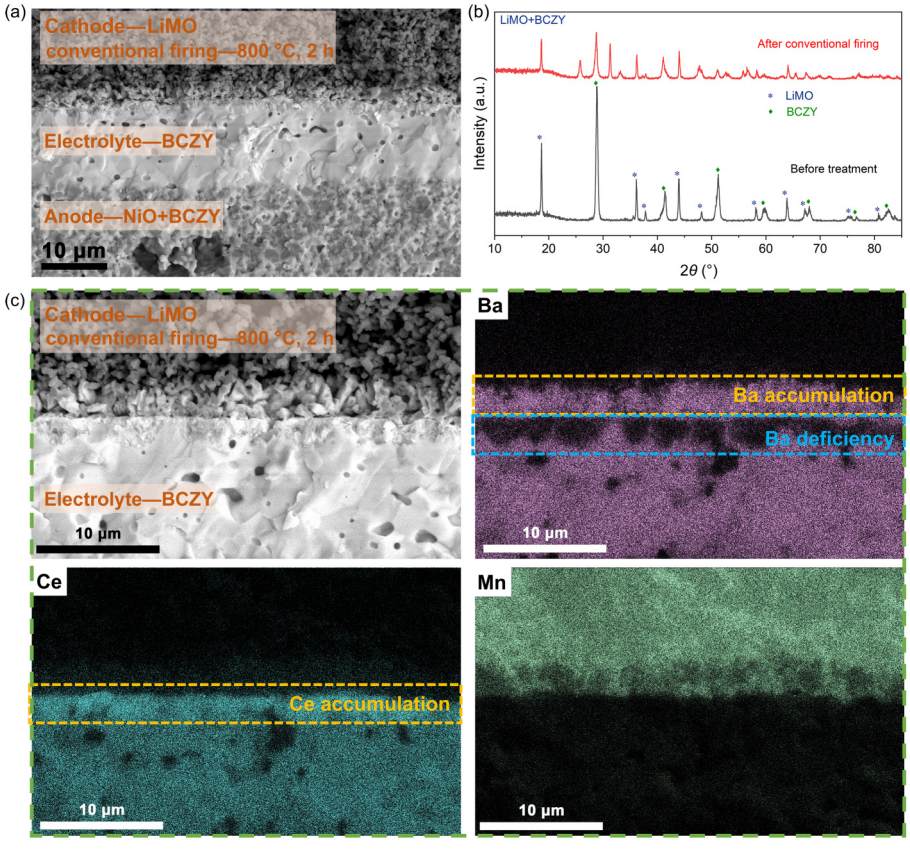

Fig. 6 (a) Cross-sectional view of cell with LiMO cathode fabricated by the conventional sintering method; (b) XRD patterns of LiMO+BCZY before and after co-firing; (c) cross-sectional view of LiMO cathode/BCZY electrolyte interface and its corresponding elemental mapping.

accumulation can be detected in the BCZY electrolyte. All suggests that the conventional co-firing approach generates an interfacial reaction between the LiMO cathode and BCZY electrolyte.

In contrast to the obvious interfacial reaction induced by conventional sintering, Joule heating can prevent unwanted reactions at the interface. Unlike a conventional co-firing operation, which takes a few hours, the Joule heating method can reach high temperatures in just a few seconds and complete co-firing in a fairly short time. In this investigation, the cathode and half-cell were co-fired at high temperatures for only 10 s. Owing to the short duration of the entire co-firing process, the interfacial reaction may be diminished. Figures 7(a) and 7(b) depict the SEM images of the cross-sectional view for LiMO cathode co-fired at 800 °C via Joule heating. The cathode adheres to the electrolyte, but there are tiny gaps between the cathode and electrolyte, indicating that the cathode and electrolyte are not in excellent contact. The TEC of LiMO is measured to be 12.25×10^{-6} °C^{-1}, as indicated in Fig. S2 in the ESM. The value is similar to that of the BCZY proton-conducting electrolyte, which is 11.09×10^{-6} °C^{-1} [41], suggesting that the LiMO material has good thermal expansion compatibility with the BCZY electrolyte. Therefore, the poor contact between LiMO cathode and BCZY illustrated above is due to an insufficient co-firing temperature rather than a thermal mismatch. Figure 7(c) shows that increasing the co-firing temperature to 850 °C causes the LiMO cathode layer to attach tightly to the electrolyte without any gaps. More crucially, no discernible interlayers can be seen at the cathode/electrolyte interface. Joule heating has the advantage of shortening the co-firing time, hence minimizing the interfacial reaction between LiMO and BCZY. To further demonstrate the chemical compatibility of LiMO and BCZY, the LiMO+BCZY composite powder was co-fired with Joule heating, using the same thermal treatment process as the cathode layer at 850 °C. Figure 7(d) depicts the XRD analysis results of the composite powder's phase composition before and after treatment. The phases of LiMO and BCZY remain unaltered following co-firing using Joule heating, as opposed to the conventional co-firing process, which produces obvious new phases. The elemental mapping results in Fig. 7(e) also reveal that there is no interfacial element diffusion. There is no evidence of Ba diffusion from the electrolyte layer to the LiMO cathode layer, although this is the case with conventional sintering process-prepared fuel cells. All of these findings support the use of Joule heating to overcome the interfacial reactivity problem between LiMO and BCZY during high-temperature co-firing operation. Moreover, the cathode and electrolyte can maintain good contact. One can wonder if the traditional sintering procedure with a very short dwell time can achieve the same result. For comparison, the LiMO cathode was co-fired with the half-cell at 850 °C for 10 s via the conventional sintering procedure, and Fig. S3 in the ESM shows a cross-section of the cell. The LiMO cathode is poorly connected to the electrolyte membrane, indicating that short dwelling time is insufficient for connecting the cathode to the electrolyte using the conventional sintering procedure. This could also explain why a few hours of dwelling time is typically needed to co-sinter the cathode and half-cell using the conventional sintering strategy.

Given that the Joule heating approach solves the interfacial reaction problem, it is worthwhile to explore the performance of LiMO as a cathode for H-SOFCs. Figure 8(a) depicts the performance of the fuel cell utilizing the LiMO built up through Joule heating. The peak power density (PPD) of the cell is 567, 982, and 1425 mW·cm^{-2} at 600, 650, and 700 °C, respectively.

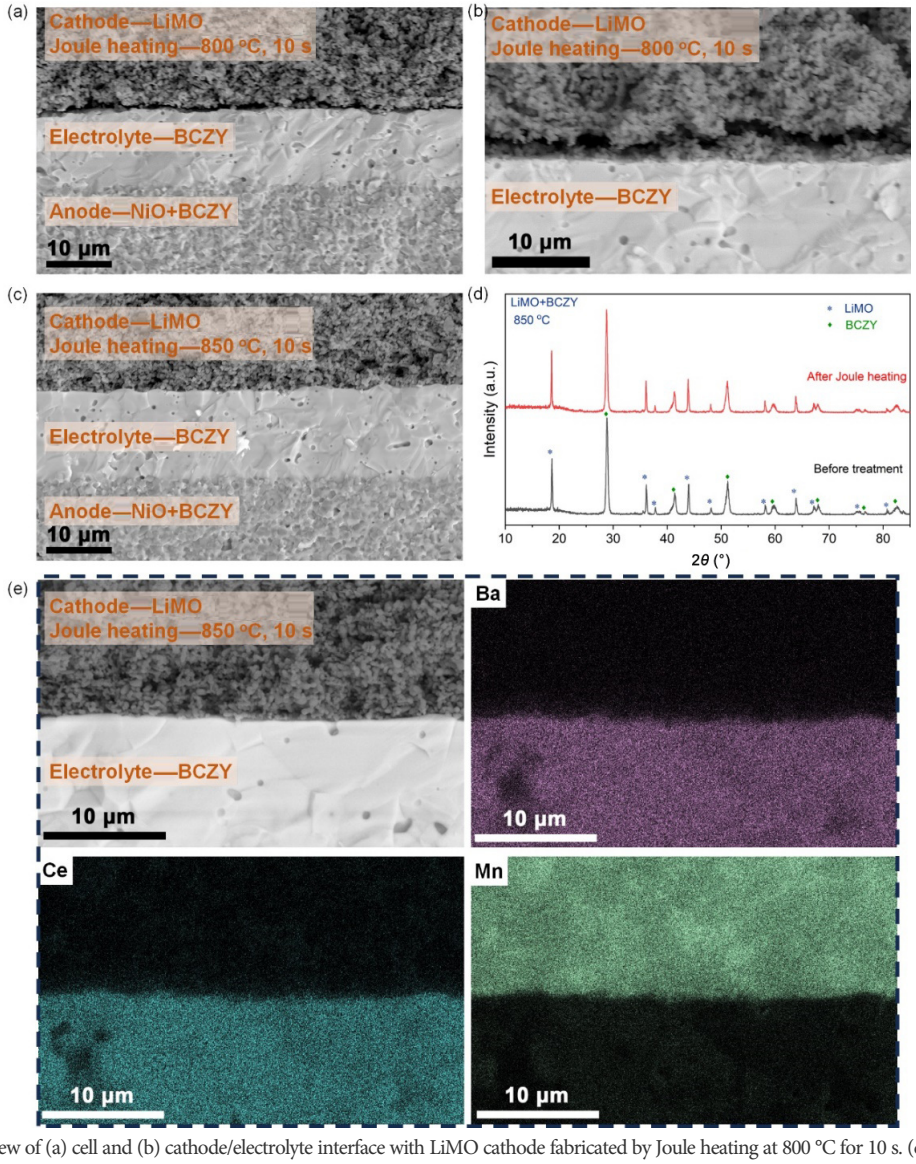

Fig. 7 Cross-sectional view of (a) cell and (b) cathode/electrolyte interface with LiMO cathode fabricated by Joule heating at 800 °C for 10 s. (c) Cross-sectional view of cell with LiMO cathode fabricated by Joule heating at 850 °C for 10 s. (d) XRD patterns for LiMO+BCZY before and after co-firing with Joule heating. (e) Cross-sectional view of LiMO cathode/BCZY electrolyte interface fabricated by Joule heating and its corresponding elemental mapping.

Good performance is expected because LiMO has exhibited significant protonation, proton diffusion ability, and conductivity, all of which are important criteria for H-SOFC cathodes. The LiMO material has not been employed in SOFCs for a long time, most likely because of its reactivity with proton-conducting electrolytes during the co-firing production process. To investigate the effect of the interfacial reaction on fuel cell performance, a fuel cell with a LiMO cathode manufactured using the conventional co-firing method is evaluated under fuel cell operating conditions, and the results are presented in Fig. 8(b). The PPD of the cell is 275, 482, and 789 mW·cm^{-2} at 600, 650, and 700 °C, respectively, which is much lower than that of the cell with the LiMO cathode formed via Joule heating. The decreased performance is most likely due to interfacial interactions, which cause the production of some undesired phases, compromising the good performance of LiMO cathode. The traditional sintering procedure produces a substantial amount of $BaMnO_3$ phase at the cathode/electrolyte interface. It has been reported that single-phase $BaMnO_3$ cathodes for H-SOFCs perform poorly and have low conductivity [49]. $BaMnO_3$ is frequently utilized in conjunction with a highly conductive cathode. Given the relatively low conductivity of LiMO described in this study, the creation of additional $BaMnO_3$ could have a detrimental effect on the cathode. Furthermore, the reaction between LiMO and BCZY causes the creation of $BaMnO_3$, implying that some Mn element in LiMO merges with Ba, resulting in Mn deficit in LiMO. The loss of transition metal Mn in LiMO may further reduce its conductivity and catalytic activity. Figure 8(c) depicts the EIS plots of fuel cells with a LiMO cathode fabricated using conventional firing and Joule heating. At 700 °C, the ohmic resistance (R_o) of the cells manufactured using conventional firing and Joule heating is 0.165 and 0.152 Ω·cm^2, respectively, with only a minor variation. Under identical testing conditions, conventional firing and Joule heating yield polarization resistance (R_p) values of 0.179 and 0.043 Ω·cm^2, respectively. The interlayer generated by the LiMO and BCZY two-phase reactions is clearly unwanted, as it reduces the cathode catalytic activity and hence increases the R_p and overall resistance of the cell. As a result, the LiMO cathode co-fired using the Joule heating approach produces more fuel cell output than the same cathode fabricated using the conventional sintering method, as illustrated in Fig. 8(d). Additionally, the performance of fuel cells using Joule heating-prepared LiMO cathodes is comparable to or

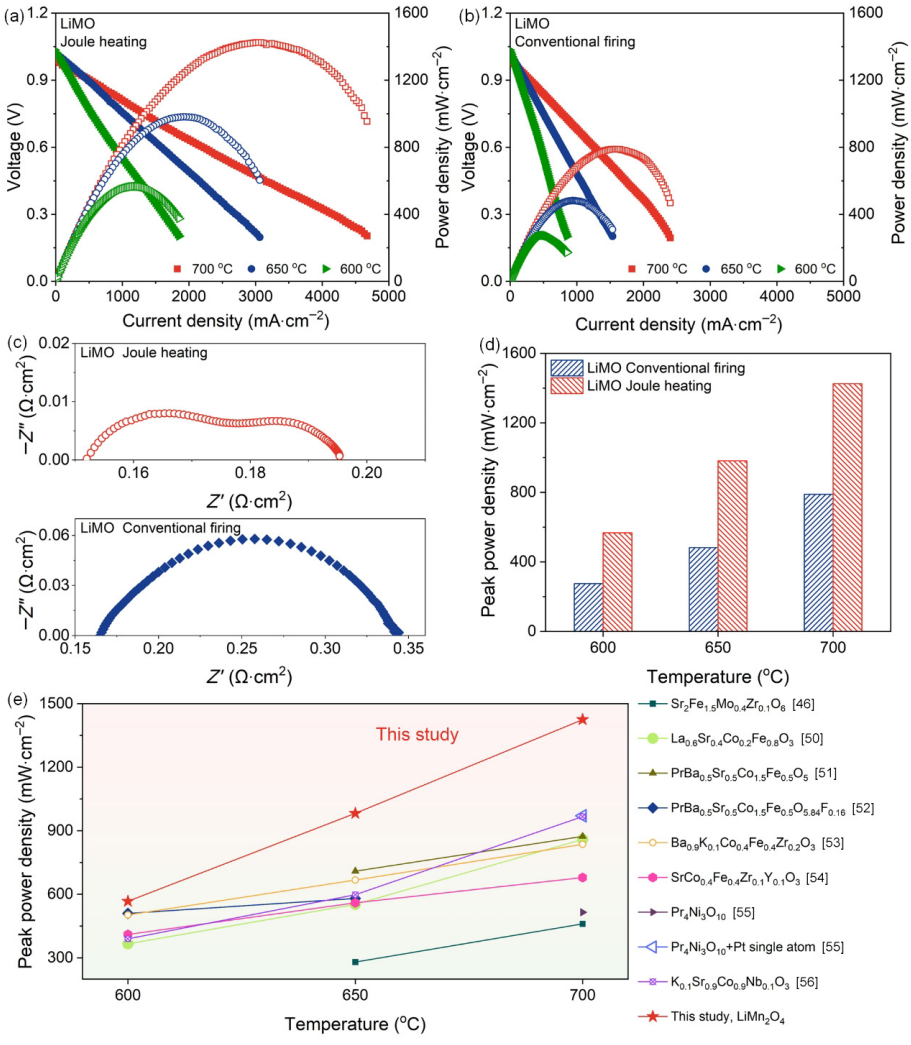

Fig. 8 Performance of fuel cells using LiMO cathode prepared by (a) Joule heating and (b) conventional sintering. (c) EIS plots of two cells tested at 700 °C. (d) PPD comparison between Joule heating and conventional heating-prepared fuel cells. (e) Performance comparison of current LiMO cell with other H-SOFCs using perovskite-based cathodes.

even better than that of many perovskite cathodes for H-SOFCs [46,50–56], as shown in Fig. 8(e), indicating the benefit of adopting a LiMO cathode. The protonation and manufacturing practicality of LiMO, which is inherited from Li-ion batteries, make it a suitable cathode contender for future H-SOFC applications. Although the current performance of lithiated oxide cathodes is still inferior to that of some recently developed high-performing perovskite cathodes [17,34,57,58], the high performance of perovskite cathodes is the result of extensive research into microstructure and composition optimization. Compared with the long history of employing perovskite cathodes in H-SOFCs [59,60], the use of lithiated oxide cathodes in H-SOFCs is new, offering possibilities for further advancement.

Because of the possibility of Li evaporation [32], one may be concerned with the stability of LiMO at operating temperatures. To test this, the LiMO powder was calcined at 600 °C for 100 h, and XRD was used to evaluate the powder's phase composition before and after long-term calcination, as shown in Fig. S4 in the ESM. After 100 h of thermal treatment at 600 °C, the LiMO powder shows no signs of new phase formation. Furthermore, no noticeable peak shift can be observed between the LiMO powder before and after thermal treatment, indicating that the LiMO phase is stable at the H-SOFC working temperature. Furthermore, the LiMO cathode has demonstrated good operational stability under fuel cell working conditions. Figure 9(a) depicts the long-term stability test for a fuel cell with a LiMO cathode made by Joule heating. The voltage of the cell remains steady for more than 150 h with a constant current density of 200 mA·cm^{-2}, suggesting that the fuel cell performs well under working conditions. The EIS plots of the cell before and after the long-term stability test are also exhibited in the figure, indicating that there is no increase in the resistance of the cell, which could be the reason for the good long-term stability. Although no interfacial diffusion was identified between the LiMO cathode and BCZY electrolyte after co-firing at 850 °C by Joule heating, one would ask if interfacial diffusion could occur at the working temperature over time. As a result, the elemental distribution is identified at the LiMO cathode/BCZY electrolyte interface after 100 h of co-firing at 600 °C, as illustrated in Fig. 9(b). There is no obvious elemental diffusion between the LiMO cathode and BCZY electrolyte, implying that LiMO and BCZY are compatible at the operating temperature of fuel cell.

In addition to the interfacial elemental distribution, the possible long-term reaction between LiMO and BCZY at H-SOFC working temperatures was studied via XRD. The LiMO and BCZY composite powders were co-fired at 600 °C for 100 h, and XRD was used to examine the phase of the powder before and after co-firing. The results shown in Fig. S5(a) in the ESM indicate that the main phases of LiMO and BCZY remain, but some minor

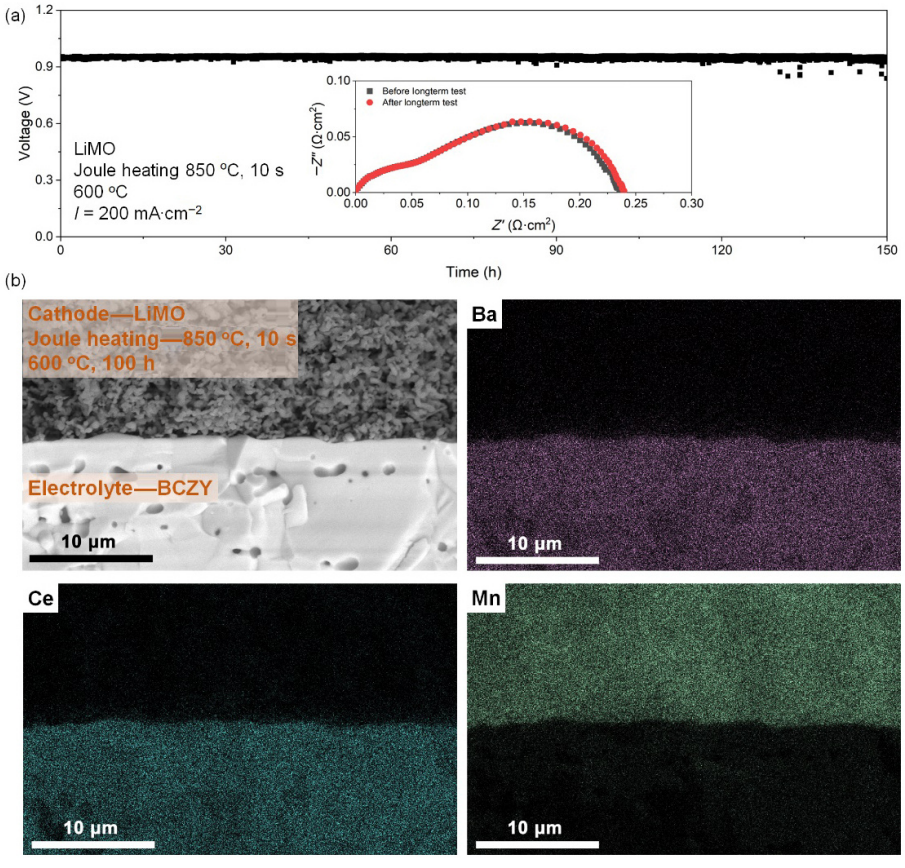

Fig. 9 (a) Long-term stability of cell with Joule heating-prepared LiMO cathode tested at 600 °C; (b) cross-sectional view of LiMO cathode/BCZY electrolyte interface after treatment at 600 °C for 100 h.

peaks appear, suggesting that some minor reactions occur between LiMO and BCZY at 600 °C for 100 h. In contrast, the reaction is more profound if the LiMO+BCZY composite powder is co-fired at a high temperature (700 °C) for 100 h. Figure S5(b) in the ESM shows the XRD patterns of the LiMO+BCZY composite powder before and after co-firing at 700 °C for 100 h. Apparent new peaks appear, and the degree of the reaction is much greater than that of the sample co-fired at 600 °C, indicating that the reaction between LiMO and BCZY is accelerated with increasing temperature. A strong reaction between LiMO and BCZY is confirmed after co-firing at 700 °C for 100 h, and the reaction is minor when the temperature is reduced to 600 °C. It seems that the working temperature of 600 °C might be sufficient for LiMO, but the working temperature of 700 °C is high enough to cause interfacial reactions. However, we further checked the long-term operational stability of the cell even at 700 °C and found that the cell worked stably for 50 h without evident degradation, as shown in Fig. S6 in the ESM. This result contradicts the XRD analysis, implying that there are other factors that should be considered.

Notably, the above chemical compatibility test was performed for LiMO and BCZY powders. In a real fuel cell, the LiMO cathode powder layer is in contact with the dense BCZY electrolyte membrane. Compared with the powder form, the dense membrane is less reactive [61]. Therefore, examining the chemical compatibility between the LiMO cathode powder and the dense BCZY electrolyte is necessary. To achieve this goal, the LiMO cathode slurry was painted on the surface of the dense BCZY electrolyte membrane, which was then co-fired at 600 and 700 °C for 100 h, respectively. After co-firing, the LiMO cathode layer was removed from the dense BCZY electrolyte membrane, and the cathode powder was collected. XRD was used to examine the phase of the LiMO cathode powder and the BCZY electrolyte membrane after co-firing. Figure S7(a) in the ESM shows the XRD patterns of LiMO powder and BCZY electrolyte membrane before and after co-firing at 600 °C. Unlike the slight reaction detected between LiMO and BCZY powders, as mentioned above, no extra peak can be observed between the LiMO powder and BCZY electrolyte membrane after co-firing. In addition, no peak shift in the XRD patterns further confirms their good chemical compatibility. Similar results are obtained for the LiMO powder and BCZY electrolyte membrane after co-firing at 700 °C, as shown in Fig. S7(b) in the ESM. Although their powder forms have reacted, the dense BCZY electrolyte membrane is more inert than the powder towards the two-phase reaction, making the phases of LiMO cathode powder and BCZY electrolyte membrane remain unchanged even after high-temperature firing. In other words, the slow reaction kinetics between the LiMO cathode powder and BCZY electrolyte membrane allow both phases to remain relatively stable even after co-firing for a long period. However, considering the very minor reaction between LiMO and BCZY, even in the powder form at 600 °C, it might be more reasonable to keep the application of LiMO for H-SOFCs at approximately 600 °C instead of at higher temperatures.

It can be concluded that using the Joule heating approach can solve the LiMO/BCZY interfacial reaction problem during the cathode co-firing operation, allowing the catalytic activity of LiMO to be fully utilized as a cathode for H-SOFCs, resulting in high fuel cell performance. Furthermore, there is no discernible interfacial diffusion between LiMO and BCZY at the H-SOFC working temperature, which is much lower than the co-firing fabrication temperature, allowing the fuel cell with the LiMO

cathode to demonstrate good operational stability. When combined with the Joule heating method, LiMO shows significant potential as a high-performance cathode, providing additional material options for H-SOFCs. Aside from Joule heating, microwave sintering is a fast-sintering approach that can reduce interfacial reactions but at slower heating and cooling rates [62]. Furthermore, cathode production using electrochemical polarization avoids high-temperature sintering while maintaining the ideal cathode morphology [63,64]. These strategies, along with the Joule heating presented in this paper, provide fascinating ways to avoid/mitigate unwanted interfacial interactions in the cell fabrication process.

4 Conclusions

LiMO, which has never been employed in H-SOFCs before, was discovered in this work to have good protonation ability and proton diffusion rates, indicating that it has high potential as a cathode for H-SOFCs. However, using the traditional sintering process during the cathode fabrication procedure does not prevent interfacial reactivity and elemental diffusion between the LiMO cathode and electrolyte, resulting in poor LiMO cathode performance in H-SOFCs. In contrast, the Joule heating approach can prevent undesired interfacial reactions. Although a similar high co-firing temperature was used, Joule heating allowed for co-firing in a matter of seconds. Because of the short heating period, no reaction between the LiMO cathode and BCZY electrolyte can be observed, allowing the LiMO cathode to be used in high-performance H-SOFCs. The LiMO cathode outperforms many well-known perovskite cathodes in H-SOFCs. Aside from the high fuel cell output, LiMO demonstrates good operational stability under fuel cell working conditions, allowing the cell to operate for 150 h without discernible degradation. Furthermore, no interfacial elemental diffusion in cathode/electrolyte is observed at the H-SOFC working temperature for an extended period, implying that Joule heating rejuvenates the LiMO material in H-SOFCs, potentially expanding the application of this traditional material in more areas.

Acknowledgements

This work was supported by the National Natural Science Foundation of China (No. 52272216) and the Natural Science Foundation of the Jiangsu Higher Education Institutions of China (No. 24KJB430001).

Declaration of competing interest

The authors have no competing interests to declare that are relevant to the content of this article. The author Lei Bi is the Associate Editor of this journal.

Electronic Supplementary Material

Supplementary material is available in the online version of this article at https://doi.org/10.26599/JAC.2025.9221040.

References

[1] Zhang F, Liao T, Yan C, *et al.* Bioinspired designs in active metal-based batteries. *Nano Res* 2024, **17**: 587–601.

[2] Zhang F, Liao T, Qi DC, *et al.* Zn-ion ultrafluidity via bioinspired ion channel for ultralong lifespan Zn-ion battery. *Natl Sci Rev* 2024, **11**: nwae199.

[3] Zhu JX, Wen HY, Zhang H, *et al.* Recent advances in biodegradable electronics- from fundament to the next-generation multi-functional, medical and environmental device. *Sustain Mater Technol* 2023, **35**: 00530.

[4] Teng JY, Xia T, Li Q, *et al.* Advanced electrocatalytic activity of praseodymium-deficient copper-based oxygen electrodes for solid oxide fuel cells. *Int J Hydrog Energy* 2023, **48**: 27361–27370.

[5] Zhu PX, Bian WJ, Liu B, *et al.* Direct conversion of methane to aromatics and hydrogen via a heterogeneous trimetallic synergistic catalyst. *Nat Commun* 2024, **15**: 3280.

[6] Dai HL, Boulfrad S, Chu XR, *et al.* $La_{0.5-x}Sc_xSr_{0.5}MnO_{3-\delta}$ cathodes for proton-conducting solid oxide fuel cells: Taking advantage of the secondary phase. *J Adv Ceram* 2024, **13**: 1759–1770.

[7] Thyssen VV, Vilela VB, de Florio DZ, *et al.* Direct conversion of methane to C_2 hydrocarbons in solid-state membrane reactors at high temperatures. *Chem Rev* 2022, **122**: 3966–3995.

[8] Wang JC, Zhao K, Zhao JS, *et al.* A NiMo-YSZ catalyst support layer for regenerable solid oxide fuel cells running on isooctane. *Appl Energy* 2022, **326**: 119907.

[9] Wang Z, Li JW, Yuan MK, *et al.* A medium-entropy engineered double perovskite oxide for efficient and CO_2-tolerant cathode of solid oxide fuel cells. *Sustain Mater Technol* 2024, **40**: e00969.

[10] Liu F, Deng H, Wang ZX, *et al.* Synergistic effects of *in situ* exsolved Ni-Ru bimetallic catalyst on high-performance and durable direct-methane solid oxide fuel cells. *J Am Chem Soc* 2024, **146**: 4704–4715.

[11] Huan DM, Zhang L, Zhu K, *et al.* Improving Ruddlesden-Popper electrocatalysts through interstitial fluorination-driven rearrangements of local coordination environment. *Sustain Mater Technol* 2023, **38**: e00754.

[12] Brett DJL, Atkinson A, Brandon NP, *et al.* Intermediate temperature solid oxide fuel cells. *Chem Soc Rev* 2008, **37**: 1568–1578.

[13] Yang ZB, Xia T, Dong ZW, *et al.* Considerable oxygen reduction activity and durability of BaO nanoparticles-decorated $Ln_{0.94}BaCo_2O_{5+\delta}$ electrocatalysts. *Sep Purif Technol* 2023, **317**: 123936.

[14] Gao Y, Ling YH, Wang XX, *et al.* Sr-deficient medium-entropy $Sr_{1-x}Co_{0.5}Fe_{0.2}Ti_{0.1}Ta_{0.1}Nb_{0.1}O_{3-\delta}$ cathodes with high Cr tolerance for solid oxide fuel cells. *Chem Eng J* 2024, **479**: 147665.

[15] Chen ZY, Jiang LZ, He S, *et al.* Development of intertwined nanostructured multi-phase air electrodes for efficient and durable reversible solid oxide cells. *Appl Catal B—Environ* 2022, **305**: 121056.

[16] Chen M, Xie XB, Guo JH, *et al.* Space charge layer effect at the platinum anode/$BaZr_{0.9}Y_{0.1}O_{3-\delta}$ electrolyte interface in proton ceramic fuel cells. *J Mater Chem A* 2020, **8**: 12566–12575.

[17] Wang Z, Wang YH, Wang J, *et al.* Rational design of perovskite ferrites as high-performance proton-conducting fuel cell cathodes. *Nat Catal* 2022, **5**: 777–787.

[18] Chen M, Chen DC, Wang K, *et al.* Densification and electrical conducting behavior of $BaZr_{0.9}YO_{3-\delta}$ proton conducting ceramics with NiO additive. *J Alloys Compd* 2019, **781**: 857–865.

[19] Zhou MY, Liu ZJ, Chen ML, *et al.* Electrochemical performance and chemical stability of proton-conducting $BaZr_{0.8-x}Ce_xY_{0.2}O_{3-\delta}$ electrolytes. *J Am Ceram Soc* 2022, **105**: 5711–5724.

[20] Feng FX, Yang WY, Zheng QL, *et al.* Tuning the oxygen vacancy of the $SrSc_{0.175}Nb_{0.025}Co_{0.8}O_{3-\delta}$ cathode toward enhanced oxygen reduction reaction for H^+-SOFCs by water uptake. *Energy Fuels* 2021, **35**: 8953–8960.

[21] Yin YR, Zhou YB, Gu YY, *et al.* Successful preparation of $BaCo_{0.5}Fe_{0.5}O_{3-\delta}$ cathode oxide by rapidly cooling allowing for high-performance proton-conducting solid oxide fuel cells. *J Adv Ceram* 2023, **12**: 587–597.

[22] Ding HP, Wu W, Jiang C, *et al.* Self-sustainable protonic ceramic electrochemical cells using a triple conducting electrode for hydrogen and power production. *Nat Commun* 2020, **11**: 1907.

[23] Wang N, Tang CM, Du L, *et al.* Advanced cathode materials for protonic ceramic fuel cells: Recent progress and future perspectives. *Adv Energy Mater* 2022, **12**: 2201882.

[24] Zhang YD, Zhu AK, Guo YM, *et al.* Electrochemical performance and effect of moisture on $Ba_{0.5}Sr_{0.5}Sc_{0.175}Nb_{0.025}Co_{0.8}O_{3-\delta}$ oxide as a promising electrode for proton-conducting solid oxide fuel cells. *Appl Energy* 2019, **238**: 344–350.

[25] Tarutina LR, Gordeeva MA, Matkin DE, *et al.* Why do $BaCo_{0.4}Fe_{0.4}$

$Zr_{0.1}Y_{0.1}O_{3-\delta}$-derived complex oxides become one of the most promising electrodes for protonic ceramic electrochemical cells. An explanatory review. *Chem Eng J* 2024, **490**: 151615.
[26] Song YF, Chen YB, Wang W, *et al.* Self-assembled triple-conducting nanocomposite as a superior protonic ceramic fuel cell cathode. *Joule* 2019, **3**: 2842–2853.
[27] Xi XA, Liu JW, Luo WZ, *et al.* Unraveling the enhanced kinetics of $Sr_2Fe_{1+x}Mo_{1-x}O_{6-\delta}$ electrocatalysts for high-performance solid oxide cells. *Adv Energy Mater* 2021, **11**: 2102845.
[28] Beshiwork BA, Wan XY, Xu M, *et al.* A defective iron-based perovskite cathode for high-performance IT-SOFCs: Tailoring the oxygen vacancies using Nb/Ta co-doping. *J Energy Chem* 2024, **88**: 306–316.
[29] Xu YS, Xu X, Bi L. A high-entropy spinel ceramic oxide as the cathode for proton-conducting solid oxide fuel cells. *J Adv Ceram* 2022, **11**: 794–804.
[30] Li YF, Xu YS, Yin YR, *et al.* Entropy engineering design of high-performing lithiated oxide cathodes for proton-conducting solid oxide fuel cells. *J Adv Ceram* 2023, **12**: 2017–2031.
[31] Yusoff WNAW, Somalu MR, Baharuddin NA, *et al.* Enhanced performance of lithiated cathode materials of $LiCo_{0.6}X_{0.4}O_2$ (X = Mn, Sr, Zn) for proton-conducting solid oxide fuel cell applications. *Int J Energy Res* 2020, **44**: 11783–11793.
[32] Xu YS, Yu SF, Yin YR, *et al.* Taking advantage of Li-evaporation in $LiCoO_2$ as cathode for proton-conducting solid oxide fuel cells. *J Adv Ceram* 2022, **11**: 1849–1859.
[33] Zeng WH, Xia FJ, Wang J, *et al.* Entropy-increased $LiMn_2O_4$-based positive electrodes for fast-charging lithium metal batteries. *Nat Commun* 2024, **15**: 7371.
[34] Choi S, Kucharczyk CJ, Liang YG, *et al.* Exceptional power density and stability at intermediate temperatures in protonic ceramic fuel cells. *Nat Energy* 2018, **3**: 202–210.
[35] Kresse G, Furthmüller J. Efficient iterative schemes for *ab initio* total-energy calculations using a plane-wave basis set. *Phys Rev B* 1996, **54**: 11169–11186.
[36] Henkelman G, Uberuaga BP, Jónsson H. A climbing image nudged elastic band method for finding saddle points and minimum energy paths. *J Chem Phys* 2000, **113**: 9901–9904.
[37] Zheng L, Ambrosetti M, Beretta A, *et al.* Electrified CO_2 valorization driven by direct Joule heating of catalytic cellular substrates. *Chem Eng J* 2023, **466**: 143154.
[38] Lee YL, Kleis J, Rossmeisl J, *et al.* Prediction of solid oxide fuel cell cathode activity with first-principles descriptors. *Energy Environ Sci* 2011, **4**: 3966–3970.
[39] Tao SW, Irvine JTS. A redox-stable efficient anode for solid-oxide fuel cells. *Nat Mater* 2003, **2**: 320–323.
[40] Wang N, Hinokuma S, Ina T, *et al.* Mixed proton–electron–oxide ion triple conducting manganite as an efficient cobalt-free cathode for protonic ceramic fuel cells. *J Mater Chem A* 2020, **8**: 11043–11055.
[41] Yin YR, Xiao DD, Wu S, *et al.* A real proton-conductive, robust, and cobalt-free cathode for proton-conducting solid oxide fuel cells with exceptional performance. *SusMat* 2023, **3**: 697–708.
[42] Han DD, Uemura DS, Hiraiwa DC, *et al.* Detrimental effect of sintering additives on conducting ceramics: Yttrium-doped barium zirconate. *ChemSusChem* 2018, **11**: 4102–4113.
[43] Kreuer KD. Proton-conducting oxides. *Annu Rev Mater Res* 2003, **33**: 333–359.
[44] Wang ZB, Yang WQ, Zhu ZY, *et al.* First-principles study of O_2 reduction on $BaZr_{1-x}Co_xO_3$ cathodes in protonic-solid oxide fuel cells. *J Mater Chem A* 2014, **2**: 16707–16714.
[45] Xia YP, Jin ZZ, Wang HQ, *et al.* A novel cobalt-free cathode with triple-conduction for proton-conducting solid oxide fuel cells with unprecedented performance. *J Mater Chem A* 2019, **7**: 16136–16148.
[46] Ren RZ, Wang ZH, Meng XG, *et al.* Tailoring the oxygen vacancy to achieve fast intrinsic proton transport in a perovskite cathode for protonic ceramic fuel cells. *ACS Appl Energy Mater* 2020, **3**: 4914–4922.
[47] Zhang LL, Yin YR, Xu YS, *et al.* Tailoring $Sr_2Fe_{1.5}Mo_{0.5}O_{6-\delta}$ with Sc as a new single-phase cathode for proton-conducting solid oxide fuel cells. *Sci China Mater* 2022, **65**: 1485–1494.
[48] Liu B, Li ZB, Yang XW, *et al.* Novel mixed $H^+/e^-/O^{2-}$ conducting cathode material $PrBa_{0.9}K_{0.1}Fe_{1.9}Zn_{0.1}O_{5+\delta}$ for proton-conducting solid oxide fuel cells. *J Mater Chem A* 2022, **10**: 17425–17433.
[49] Zhou R, Yin YR, Dai HL, *et al.* Attempted preparation of $La_{0.5}Ba_{0.5}MnO_{3-\delta}$ leading to an *in-situ* formation of manganate nanocomposites as a cathode for proton-conducting solid oxide fuel cells. *J Adv Ceram* 2023, **12**: 1189–1200.
[50] Xu YS, Gu YY, Bi L. A highly-active $Zn_{0.58}Co_{2.42}O_4$ spinel oxide as a promising cathode for proton-conducting solid oxide fuel cells. *J Mater Chem A* 2022, **10**: 25437–25445.
[51] Bai H, Chu JM, Chen T, *et al.* $PrBa_{0.5}Sr_{0.5}Co_{1.5}Fe_{0.5}O_{5+\delta}$ as air electrode for proton-conducting solid oxide cells. *J Power Sources* 2023, **574**: 233162.
[52] Xu Y, Huang YL, Guo YM, *et al.* Engineering anion defect in perovskite oxyfluoride cathodes enables proton involved oxygen reduction reaction for protonic ceramic fuel cells. *Sep Purif Technol* 2022, **290**: 120844.
[53] Qiu P, Liu B, Wu L, *et al.* K-doped $BaCo_{0.4}Fe_{0.4}Zr_{0.2}O_{3-\delta}$ as a promising cathode material for protonic ceramic fuel cells. *J Adv Ceram* 2022, **11**: 1988–2000.
[54] Lv XQ, Chen HL, Zhou W, *et al.* $SrCo_{0.4}Fe_{0.4}Zr_{0.1}Y_{0.1}O_{3-\delta}$, a new CO_2 tolerant cathode for proton-conducting solid oxide fuel cells. *Renew Energy* 2022, **185**: 8–16.
[55] Li XY, Chen ZM, Yang Y, *et al.* Highly stable and efficient Pt single-atom catalyst for reversible proton-conducting solid oxide cells. *Appl Catal B—Environ* 2022, **316**: 121627.
[56] Zhu K, Yang Y, Huan DM, *et al.* Theoretical and experimental investigations on K-doped $SrCo_{0.9}Nb_{0.1}O_{3-\delta}$ as a promising cathode for proton-conducting solid oxide fuel cells. *ChemSusChem* 2021, **14**: 3876–3886.
[57] Yin YR, Wang YF, Yang N, *et al.* Unveiling the importance of the interface in nanocomposite cathodes for proton-conducting solid oxide fuel cells. *Exploration* 2024, **4**: 20230082.
[58] Dai HL, Wang LL, Boulfrad S, *et al.* Combining $La_{0.5}Sr_{0.5}MnO_{3-\delta}$ cathode with a mixed conductor towards enhanced performance of proton-conducting solid oxide fuel cells. *Chem Eng J* 2024, **502**: 158036.
[59] Dai HL, Du HZ, Boulfrad S, *et al.* Manipulating Nb-doped $SrFeO_{3-\delta}$ with excellent performance for proton-conducting solid oxide fuel cells. *J Adv Ceram* 2024, **13**: 579–589.
[60] Dong XC, Yu SF, Gu YY, *et al.* Tailoring $SrFeO_3$ cathode with Ta and F allows high performance for proton-conducting solid oxide fuel cells. *Sustain Mater Technol* 2024, **41**: 01104.
[61] Bi L, Zhang SQ, Fang SM, *et al.* A novel anode supported $BaCe_{0.7}Ta_{0.1}Y_{0.2}O_{3-\delta}$ electrolyte membrane for proton-conducting solid oxide fuel cell. *Electrochem Commun* 2008, **10**: 1598–1601.
[62] Liu ZL, Yu SF, Wang M, *et al.* Mitigating anode/electrolyte interfacial Ni diffusion by a microwave sintering method for proton-conducing solid oxide fuel cells. *Electrochem Commun* 2023, **155**: 107583.
[63] Chen ZY, Jiang LZ, Yue ZW, *et al.* Facile approach for improving the interfacial adhesion of nanofiber air electrodes of reversible solid oxide cells. *ACS Appl Mater Inter* 2023, **15**: 8120–8127.
[64] Zhang FH, Weng QH, Zhang YX, *et al.* Facile preparation of electrodes of efficient electrolyte-supported solid oxide fuel cells using a direct assembly approach. *Electrochim Acta* 2022, **424**: 140643.